Structure analysis (XRD and Neutrons) and hydrogen storage properties of Hf1-Ti NbVZr BCC high entropy alloys

Maria Moussa, Lambert van Eijck, Jacques Huot, Jean-Louis Bobet

Journal of Alloys and Compounds 1010 (2025) 177103

Contents lists available at ScienceDirect

Journal of Alloys and Compounds

journal homepage: www.elsevier.com/locate/jalcom

Structure analysis (XRD and Neutrons) and hydrogen storage properties of $Hf_{1-x}Ti_xNbVZr$ BCC high entropy alloys

Maria Moussa [a,b,*], Lambert van Eijck [c], Jacques Huot [a], Jean Louis Bobet [b,**]

[a] Hydrogen Research Institute, Université du Québec à Trois-Rivières, 3351 des Forges, Trois-Rivières, QC G9A 5H7, Canada
[b] CNRS, University Bordeaux, Bordeaux INP, ICMCB, UMR 5026, Pessac 33600, France
[c] Department of Radiation Science and Technology, fac. Applied Sciences, Delft University of Technology, Mekelweg 15, Delft 2629JB, the Netherlands

ARTICLE INFO

Keywords:
High entropy alloys
BCC alloys
Dehydrogenation
X-ray diffraction
Neutron diffraction

ABSTRACT

The hydrogen storage properties of $Hf_{1-x}Ti_xNbVZr$ high entropy alloys (HEAs) synthesized by arc melting have been investigated. The first hydrogenation of the alloys was performed at room temperature under 20 bars of hydrogen pressure. Results show an increase in gravimetric hydrogen content with Ti substitutions. Upon hydrogenation, the multiphase alloys ($x = 0$ and $x = 0.25$) exhibit a combination of faces-centred-cubic (FCC) hydride and C15 Laves phases, while single-phase alloys ($x = 0.5$, 0.75, and 1) display FCC structures. The crystal structure evolution during dehydrogenation of HfNbVZr ($x = 0$) and TiNbVZr ($x = 1$) HEAs was examined using *in-situ* neutron diffraction. The analysis demonstrates temperature-dependent desorption behaviour, with HfNbVZr displaying lower desorption temperatures compared to TiNbVZr. Additionally, *in-situ* neutron diffraction experiments during deuterium desorption indicate a two-step phase transition from FCC dihydride to BCT monohydride, followed by a transition to BCC.

1. Introduction

Hydrogen is attracting interest as an energy carrier in renewable energy systems [1,2]. Hydrogen could be stored in liquid, gaseous and solid state, each of these techniques having advantages and disadvantages. In the case of the solid-state method using metal hydrides, the advantages are high volumetric storage capacities at low pressure and near room temperature [1,2].

Recently, a new class of alloys, the so-called high entropy alloys (HEA), have been investigated for their hydrogen storage properties. In these multi principal elements alloys described by Cantor *et al.* and Yeh *et al.* [3,4], the large number of elements and their random distribution on the lattice sites provides a large diversity of local environments for hydrogen atoms [5–7].

Recently, a new class of alloys, the so-called high entropy alloys (HEA), have been investigated for their hydrogen storage properties. In these multi principal elements alloys described by Cantor *et al.* and Yeh *et al.* [3,4], the large number of elements and their random distribution on the lattice sites provides a large diversity of local environments for hydrogen atoms [5–7].

HEAs often solidify in body-centered cubic (BCC) [8], face-centered cubic (FCC) [9], or hexagonal close-packed (HCP) [10] structures. Nevertheless, Laves phases, which are very common intermetallic phases having an AB_2 stoichiometry, (mainly hexagonal $MgZn_2$ (C14), cubic $MgCu_2$ (C15) and more rarely hexagonal $MgNi_2$ (C36)) are generally found alongside other phases in high-entropy alloys.

Interest has laid towards the HEA BCC alloys containing refractory elements such as Nb, V and Hf that all have melting points higher than 2000 °C. Since these individual metals can form hydrides with a large amount of hydrogen (H/M = 2), it could be expected that a combination of them would also absorb hydrogen [11]. For example, the TiVZrNbHf HEA showed an outstanding storage capacity of 2.5H/M (2.7 wt%) [12]. In order to better understand this high sorption content, several authors have tried to link the hydrogen content with the fundamental properties of the alloys like the lattice parameter, atomic mismatch (lattice distortion) [13], Valence Electron Concentration (VEC) [14], or chemical composition [15–17]. The differences in chemical composition can have strong effects on the hydrogen storage properties in the HEAs. For instance, Gustav Ek *et al.* synthesized a total of 21 HEAs in the TiVZrNbHf system with varying elemental compositions [14]. Among the synthesized alloys, 15 of them formed either face-centred-cubic (FCC) or body-centred tetragonal (BCT) metal hydrides with

* Corresponding author at: Hydrogen Research Institute, Université du Québec à Trois-Rivières, 3351 des Forges, Trois-Rivières, QC G9A 5H7, Canada.
** Corresponding author.
E-mail addresses: maria.moussa@u-bordeaux.fr (M. Moussa), jean-louis.bobet@icmcb.cnrs.fr (J.L. Bobet).

https://doi.org/10.1016/j.jallcom.2024.177103
Received 5 June 2024; Received in revised form 30 September 2024; Accepted 16 October 2024
Available online 17 October 2024

maximum H/M ratios close to 2. As the alloys underwent hydrogenation, there was a linear increase in the unit cell volume expansion per metal atom, correlating with both the valence electron concentration (VEC) and the average Pauling electronegativity of the alloys. Overall, the authors suggested the existence of a complex relationship between the chemical composition of HEAs and their corresponding hydrides in terms of hydrogen storage properties.

Zlotea *et al.* analyzed the effect of the composition on the hydrogen sorption properties by replacing only one element in the $Ti_{0.30}V_{0.25}Zr_{0.10}Nb_{0.25}M_{0.10}$ (with M = Mg, Al, Cr, Mn, Fe, Co, Ni, Cu, Zn, Mo and Ta) alloy [8]. The authors concluded that the maximum hydrogen storage capacity at room temperature strongly depends on the valence electron concentration (VEC) of the alloys: at low VEC values ($<$ 4.9) the capacity is high (1.5–2.0H/M), while at VEC $\geq$ 4.9 a drastic decrease in the capacity is observed.

Floriano *et al.* synthesized a TiZrNbCrFe HEAs by arc melting [18]. Their findings revealed that the alloy primarily consisted of a C14 Laves phase, with a minor presence of a BCC structure. The alloy demonstrated a reversible hydrogen capacity of 1.90 wt% at 200 °C.

Yadav *et al.* synthesised the high-entropy Ti–Zr–V–Cr–Ni using conventional melting and casting methods as well as the melt-spinning technique. The melt-spun TiZrVCrNi HEA ribbons achieved a total hydrogen storage capacity of approximately 2 wt% [19].

Zlotea *et al.* have shown that the hydrogen storage capacity strongly depends on VEC of the alloys [8]. As as Ti and Hf have the same number of valence electrons, the VEC for all our investigated alloys is constant and equal to 4.5, favouring a capacity of hydrogen absorption between 1.5 and 2.0H/M. This value was calculated using Eq. 1 defined in reference [20]:

$$VEC = \sum_{i=1}^{n} C_i(VEC)_i \quad (1)$$

Where $(VEC)_i$ is the VEC for the i^{th} element, which is the number of total electrons in the valence band including d electrons. The VECs for Ti, Hf, Nb, V and Zr elements are respectively 4, 4, 5, 5, and 4 [14]. C_i is the atomic percentage of the i^{th} element, and n is the number of elements in the alloy.

In the present investigation, we substituted Hf by Ti in the $Hf_{1-x}Ti_xNbVZr$ HEA. The reason for this substitution is that Ti is lighter than Hf, thus a higher gravimetric hydrogen storage capacity could be achieved by the hydrides, while still leveraging the high melting points and hydride-forming properties of the alloy components. The hydrogen storage properties including first hydrogenation and hydrogen desorption were studied. *In-situ* neutron diffraction was employed to determine the location of hydrogen atoms in the fully hydrated state and to observe the evolution of hydride phases during the dehydrogenation process in both the multiphase HfNbVZr ($x = 0$) and the single-phase TiNbVZr ($x = 1$) alloys. Additionally, ex-situ X-ray diffraction was used to further study the phase changes in these alloys.

2. Materials and methods

All the raw materials Ti (99.9 %), Hf (99.9 %), V (99.7 %), Zr (99.5 %) and Nb (99.9 %) were purchased from Alfa Aesar® and used as received. Prior to the melting, the raw elements were mixed in the desired proportion then synthesized by arc melting under 0.7 bars of argon. Each pellet was melted, turned over, and remelted five times to ensure good homogeneity. After the synthesis, the as-cast alloy was hand-crushed inside an argon-filled glove box using a hardened steel mortar and pestle.

The first hydrogenation of all alloys was measured under 20 bars of hydrogen pressure at room temperature using a home-made Sievert's type apparatus. The powder was filled in the sample holder under argon atmosphere to prevent oxidation. Prior to the hydrogenation measurement, the sample was kept under dynamic vacuum for one hour at room temperature.

The crystal structure of the hydrides and the desorbed alloys were determined by X-ray diffraction using a Bruker D8 Focus with Cu Kα radiation. Crystallographic parameters were evaluated from Rietveld refinement using the Topas software with the pseudo-Voigt profile data utilized for fitting the XRD patterns [21].

For the neutron powder diffraction experiments, the alloys were fully deuterated (*ex-situ*) at room temperature and under 20 bars of pressure. Neutron experiments were performed on the PEARL neutron powder diffractometer at the research reactor of Delft University of Technology, using the (533) reflection of the germanium monochromator (1.667 Å) [22]. The samples were placed in a vanadium container. During the neutron *in-situ* measurements, the desorption step was carried out with a constant heating rate of 2 K/min while neutron patterns were recorded every 5 minutes. Neutron diffraction patterns were analyzed by Rietveld refinement using both GSAS II and TOPAS softwares [21,23].

3. Results and discussion

3.1. As-cast samples

The microstructure and crystal structure of the as-cast samples have already been reported in detail in a previous article [24], but to better support our discussion, the corresponding BSE images are shown in the supplementary file (**Fig.S1**).

It was found that all the synthesized alloys displayed a BCC phase (Fig. 1), and their cell parameter varied between 3.311 Å and 3.392 Å. The studied alloys with low Ti concentration ($x \leq 0.25$) exhibited an additional cubic C15 phase (a = 7.376–7.460 Å). According to the results of scanning electron microscopy, two phases appeared: a dendritic one with a composition close to the nominal alloy identified as BCC, and a dark region enriched with V identified as C15 Laves phase.

The lattice parameters as a function of x is shown in Fig. 2. It is clear that the Vegard's law is respected in the $Hf_{1-x}Ti_xNbVZr$ series. For these alloys, the lattice parameter of the BCC phase decreases with increasing atomic content of Ti. This trend was expected since titanium has a smaller metallic radius than hafnium - 1.46 Å and 1.58 Å respectively. However, the bcc lattice parameters vary linearly with composition across the entire range (Fig. 2), indicating that the presence of the C15 phase does not appear to influence the bcc lattice parameter. This is expected since the matrix, associated with the cubic crystal structure, has a composition close to the nominal value.

3.2. First hydrogenation

The first hydrogenation (activation) of the $Hf_{1-x}Ti_xNbVZr$ (with x = 0–1 by step of 0.25) was performed at room temperature under 20 bars of hydrogen pressure and without any prior heat treatment.

The first hydrogenation kinetics of all the alloys investigated in this study is shown in Fig. 3 (a). As expected, the substitution of a heavy element (Hf) by a lighter one (Ti), resulted in an increase in the gravimetric hydrogen content (wt%). For the single-phase alloys, the kinetics could be represented in terms of the hydrogen to metal (H/M) ratio. This is shown in Fig. 3 (b) and indicate that substituting Hf by Ti has no impact on the number of hydrogen atoms stored in the hydride phase.

After the first hydrogenation, the crystal structure of the hydride alloys was investigated by XRD. The results are shown in Fig. 4. The crystal structure parameters and the abundance of each phase in all hydrogenated samples as determined by Rietveld's analysis are presented in Table 1.

As mentioned in a previous work [22], the as-cast alloys $x = 0$ and $x = 0.25$ are multiphase (containing BCC and small amount of C15 phase). Once hydrogenated, the crystal structure is essentially a main FCC phase with a C15 secondary Laves phase. It has been reported that FCC (or BCT) are the structures adopted by a fully hydride BCC HEA [12,18,24]. The hydrides of titanium rich alloys ($x = 0.5$, 0.75 and 1), are all single

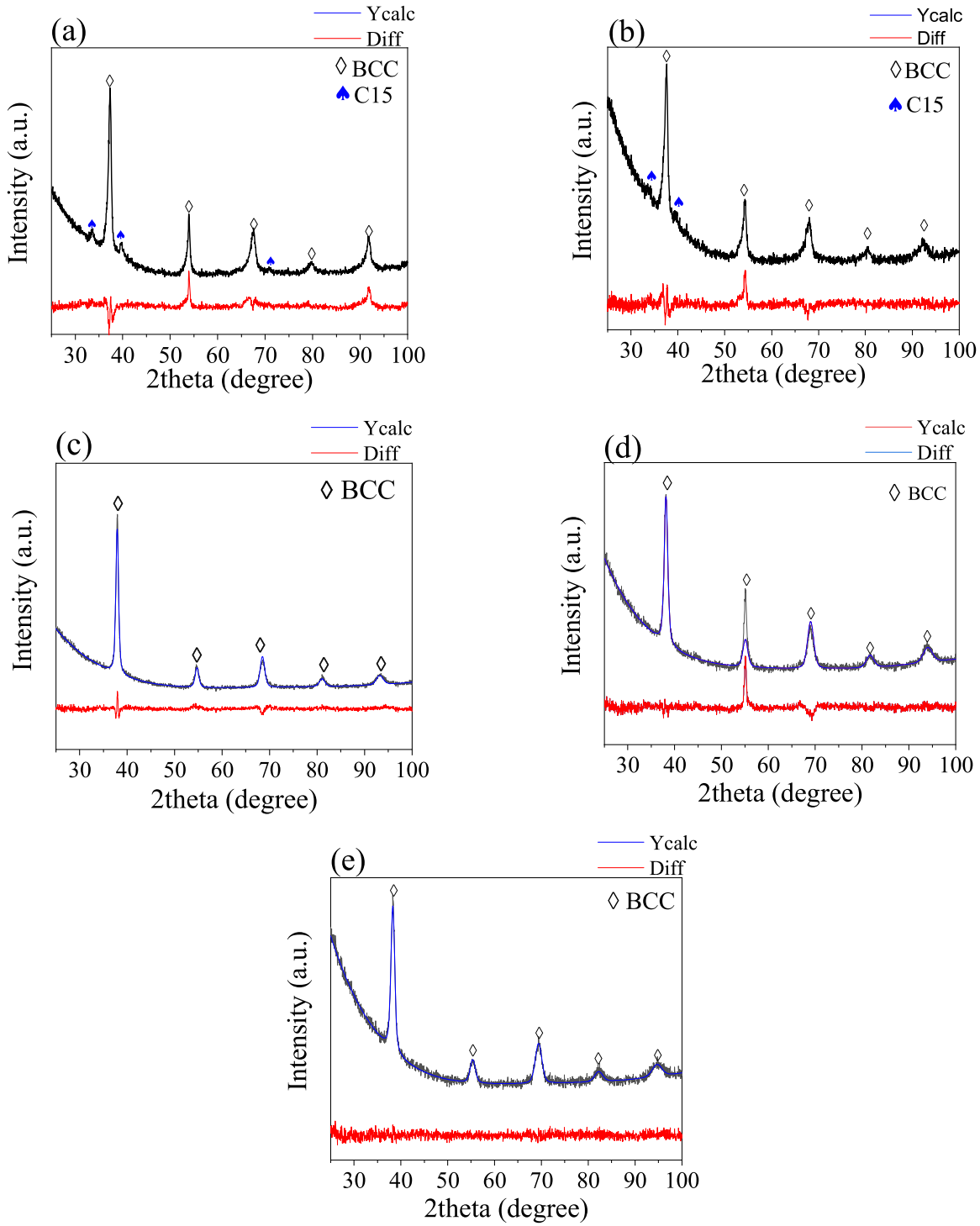

Fig. 1. XRD analysis of the $Hf_{1-x}Ti_xNbVZr$ alloys in the as-cast state for: (a) x = 0, (b) x = 0.25, (c) x = 0.5, (d) x = 0.75 and (e) x = 1. The solid black lines, blue lines and red lines express respectively the observed and calculated XRD patterns of the sample and the residue of the Rietveld refinement. Adapted from [24].

phase FCC. For all the alloys investigated in our work, we did the Rietveld refinement with both possible structures (FCC and BCT). Rietveld refinements using the FCC and BCT structures for one alloy (TiNbVZr alloy) are shown in the supplementary file (Fig. S1). This assumption was validated by neutron diffraction measurements presented later in Fig. 5. Moreover, having an FCC in the hydride state is in agreement with most of the reports on HEAs dihydrides [14,25].

As the unit cell volume of all phases in the hydride state was larger than in the as-cast state, we could use the volume increase to estimate the hydrogen content in each phase. Considering that a hydrogen atom produces a volume expansion of 2.7 $Å^3$ (as found by Peisl [26] and Sleiman *et al.* [27]) the estimated amount of hydrogen in each phase is determined from the volume expansion by unit formula (ΔV) of each hydride phase. The results are shown in Table 2. Taking into consideration the abundance of each phase in the hydrided samples, the estimated amount of hydrogen in each alloy is shown in Table 3. This table shows that the measured capacities were in in a good agreement with the estimated range.

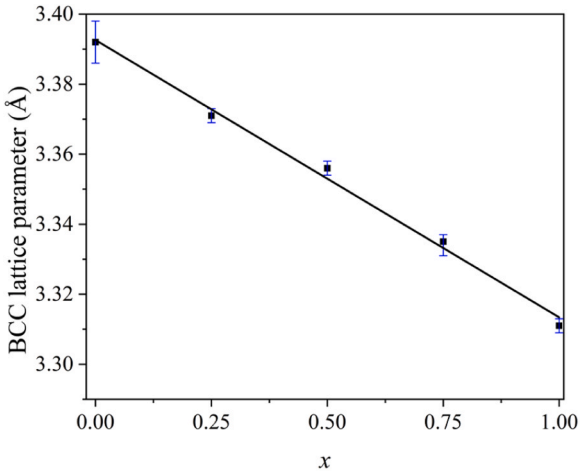

Fig. 2. Lattice parameter as a function of x for the $Hf_{1-x}Ti_xNbVZr$ alloys.

3.3. *Neutron diffraction analysis of x = 1 and x = 0 fully hydrided alloys*

For complementary structural investigation of the hydrides, the crystalline structure of the fully hydrided alloys $x = 1$ (TiNbVZr) and $x = 0$ (HfNbVZr) was studied by neutron diffraction (Fig. 5). Deuterium was used instead of hydrogen in these experiments because of the high incoherent scattering of hydrogen atoms causing significant background. This technique of characterization enables us to locate the position of deuterium atoms inside the FCC lattice of the deuteride alloy. The Rietveld analysis of the hydride TiNbVZr ($x = 1$), shows a single-phase hydride with an FCC structure (CaF_2-type $Fm\bar{3}m$) and lattice parameter $a_{FCC} = 4.518$ Å which is in relatively good agreement with the XRD results ($a_{FCC} = 4.540$ (1) Å). The deuterium atoms were located at the tetrahedral sites *8c* (¼, ¼, ¼), revealing a deuterium content of 2 D/M. This result is in agreement with previous studies on similar HEAs [28].

The hydride HfNbVZr ($x = 0$) shows a multiphase hydride with FCC and C15 structure having lattice parameters of $a_{FCC} = 4.636$ Å and $a_{C15} = 7.989$ Å, in fairly good agreement with the XRD results (Table 1, $a_{FCC} = 4.654$ (3) Å and $a_{C15} = 7.957$ (8) Å). For this alloy, the deuterium occupies the tetrahedral sites *8c* (¼, ¼, ¼) in the FCC lattice with a deuterium content of 2 D/M, while it occupies the *96 g* sites (0.060, 0.060, 0.397) in the C15 lattice having a deuterium content of 1.7 D/M. This result in agreement with the position determined by Soubeyroux *et al.* in $Zr(Cr_{1-x}M_x)_2$ with M =$(Cu_{0.5}Ni_{0.5})$ for the $0 < x < 0.2$ alloys [29].

As shown in Fig. 5, the diffraction peaks of the FCC phase in the hafnium rich alloy (HfNbVZr, $x = 0$) are obviously broader than the FCC peaks of the titanium rich alloy (TiNbVZr, $x = 1$). The peaks broadening is correlated with the crystallite size evaluated from X-ray diffraction shown in Table 1.

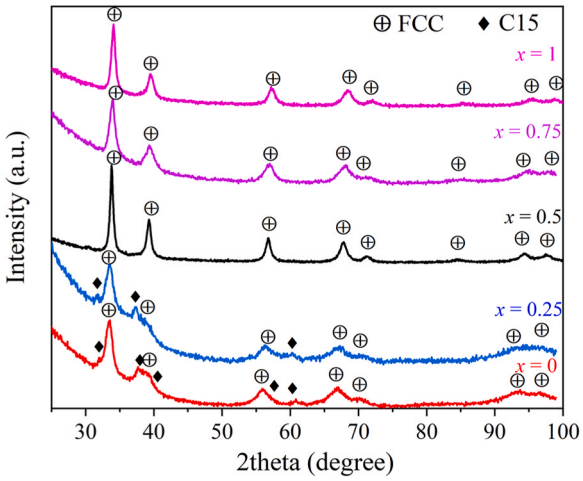

Fig. 4. XRD patterns of the $Hf_{1-x}Ti_xNbVZr$ alloys in the hydrogenated state for x = 0, 0.25, 0.5, 0.75 and 1.

Table 1
Crystal structure parameters of $Hf_{1-x}Ti_xNbVZr$ in the hydrogenated state for x = 0, 0.25, 0.5, 0.75 and 1. Error on the last significant digit is indicated between brackets.

Composition $Hf_{1-x}Ti_xNbVZr$	Phase	Lattice parameter (Å)	Cell volume (Å^3)	Crystallite size (nm)
$x = 0$	FCC (87 %)	4.654 (3)	100.8 (2)	3.4 (1)
	C15 (13 %)	7.957 (8)	504.2 (7)	5.4 (6)
$x = 0.25$	FCC (83 %)	4.637 (4)	99.7 (3)	2.6 (7)
	C15 (17 %)	7.956 (6)	504.1 (8)	—
$x = 0.5$	FCC (100 %)	4.582 (1)	96.2 (3)	13.3 (2)
$x = 0.75$	FCC (100 %)	4.576 (2)	95.8 (9)	11.4 (8)
$x = 1$	FCC (100 %)	4.540 (1)	93.6 (5)	18.2 (7)

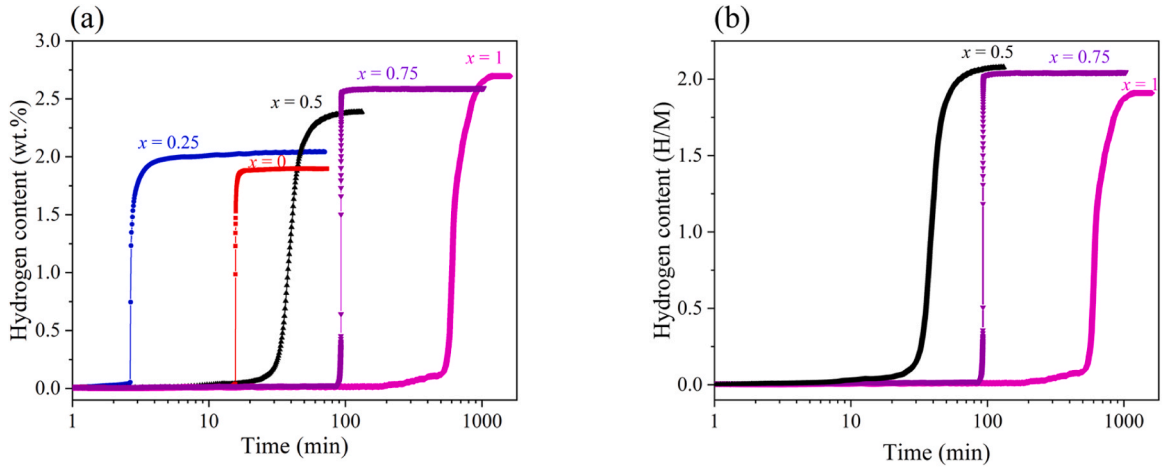

Fig. 3. Hydrogen content of $Hf_{1-x}Ti_xNbVZr$ alloy in (a) wt.% for x = 0, 0.25, 0.5, 0.75 and 1 (b) H over M ratio for x = 0.5, 0.75 and 1.

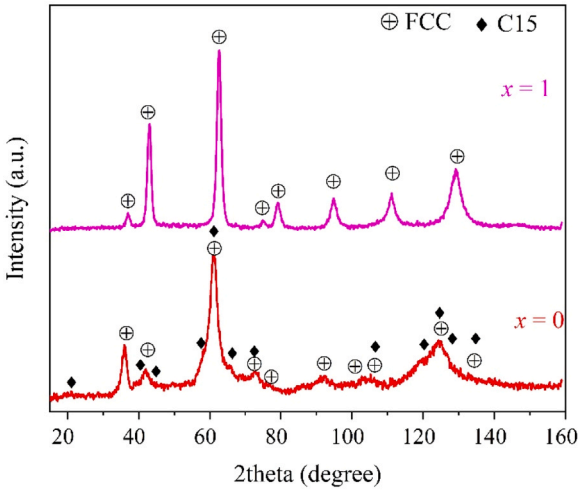

Fig. 5. Neutron powder diffraction pattern of the fully deuteried HfNbVZr (x = 0) and TiNbVZr (x = 1).

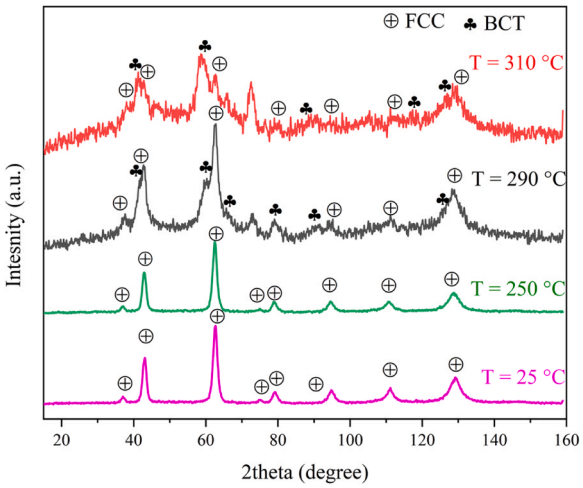

Fig. 6. Desorption neutron diffraction pattern of fully deuterated TiNbVZr alloy.

Table 2
The variation of volume per unit formula ΔV and the estimated range of hydrogen in each phase in the hydrogenated samples.

x in $Hf_{1-x}Ti_xNbVZr$ alloys	ΔV of C15 (Å^3)	Estimated amount of H in C15 (wt.%)	ΔV of FCC (Å^3)	Estimated amount of H in FCC (wt. %)
0	3.7	1.5	5.7	2.4
0.25	4.3	1.8	5.8	2.5
0.5	—	—	5.2	2.5
0.75	—	—	5.4	2.5
1	—	—	5.2	2.7

Table 3
Estimated capacity of the phases in the hydrided samples.

x in $Hf_{1-x}Ti_xNbVZr$ alloys	Estimated amount of H in the hydride (wt.%)	Measured capacity (wt.%)
0	2.3	1.9
0.25	2.3	2.1
0.5	2.5	2.4
0.75	2.5	2.6
1	2.7	2.7

After the acquisition of the fully deuterided alloys, the dehydrogenation by *in-situ* neutron diffraction and *ex-situ* XRD was performed.

3.4. Neutron diffraction analysis of x = 1 (TiNbVZr) alloy: In-situ measurements

Fig. 6 shows selected *in-situ* neutron diffraction patterns of the TiNbVZr alloy during heating from 25 °C to 310 °C under dynamic vacuum.

Rietveld refinements were performed on each pattern presented in Fig. 6. Specifically, the refined patterns of the alloy at 25 °C and 290 °C are showcased in Fig. 7 (a) and (b) respectively. The calculated parameters resulting from these refinements are presented in Table 4.

As depicted in Fig. 6 and Table 4, the diffraction patterns at 25 °C, 250 °C and 290 °C consistently reveal the primary phase as FCC. Notably, there is a gradual decrease in diffraction peak intensities from 25 °C to 290 °C. However, at 310 °C, the dominant phase is BCT (57 %) accompanied by a significant drop in peak intensity of the FCC phase. During the dehydrogenation process, the lattice parameter of the FCC crystal structure slightly increases with the temperature. This lattice expansion can be attributed to the thermal expansion caused by the temperature increase. The thermal expansion evaluated from 25 °C to 250 °C was 7.7×10^{-6} K^{-1}). This agrees with the literature values ranging from 5×10^{-6} K^{-1} to 25 $\times10^{-6}$ K^{-1} [30].

Through Rietveld refinement, the deuterium atoms are determined to occupy tetrahedral sites in both lattices ((¼ ¼ ¼) for FCC, and (0 ½ ¼) for BCT). During the heating process from 25 to 310 °C, the deuterium occupancy within the FCC lattice remains constant at 1 (*i.e.* 2 D/M), confirming it as a dihydride. At 290 °C, both BCT and FCC phases are present. However, the deuterium occupying tetrahedral sites within the BCT lattice has an occupancy of 0.6, indicating a deuterium content of 1.2 D/M (not so far from 1 D/M). This confirms that the BCT lattice is a monohydride. It is well known that upon desorption, the FCC phase (dihydride) first transforms to BCT structure (monohydride) and ultimately back to BCC phase. No BCC is seen in the patterns at 310 °C, indicating an incomplete dehydrogenation at this temperature.

3.5. X-ray Diffraction analysis of x = 1 (TiNbVZr) alloy: Ex-situ dehydrogenation

For complementary investigation of dehydrogenation of TiNbVZr alloy, *ex-situ* XRD after dehydrogenation was performed. After reaching full hydrogenation, the sample was subjected to a dynamic vacuum for two hours at 375 °C. The XRD pattern of the dehydrogenated sample is presented in Fig. 8. The crystal parameters of as-cast, fully hydrided and desorbed TiNbVZr alloy are reported in Table 5.

The pattern of the desorbed TiVZrNb ($x = 1$) alloy presented in Fig. 8, shows the presence of a single BCC phase with a cell volume of 39.30 Å^3 which is slightly larger than the as cast cell volume (36.31 Å^3). This indicates that also this sample is not fully desorbed under the applied conditions. For a hydrogen volume of 2.7 Å^3 the alloy still contains 0.78 wt% (*i.e.* 0.55 H/M). This is supported by the desorption isotherms presented in Fig S3**.** Our results are consistent with the results published by Nygard *et al.* [13], where the authors studied the *in-situ* synchrotron radiation powder X-ray diffraction measurement during desorption of hydrogen from $TiVNbZrH_2$. It was stated that for this composition, the FCC hydrides, having [H]/[M] close to 2 transforms to a BCC containing hydrogen in solid solution.

After analyzing the two alloys after dehydrogenation using *in-situ* neutron diffraction and *ex-situ* XRD techniques, a clear difference emerges: At the end of *ex-situ* dehydrogenation, the phase is a BCC one (from XRD analysis), which agrees well with the as-cast state. From the *in-situ* neutron diffraction, BCT and FCC phases are present. This

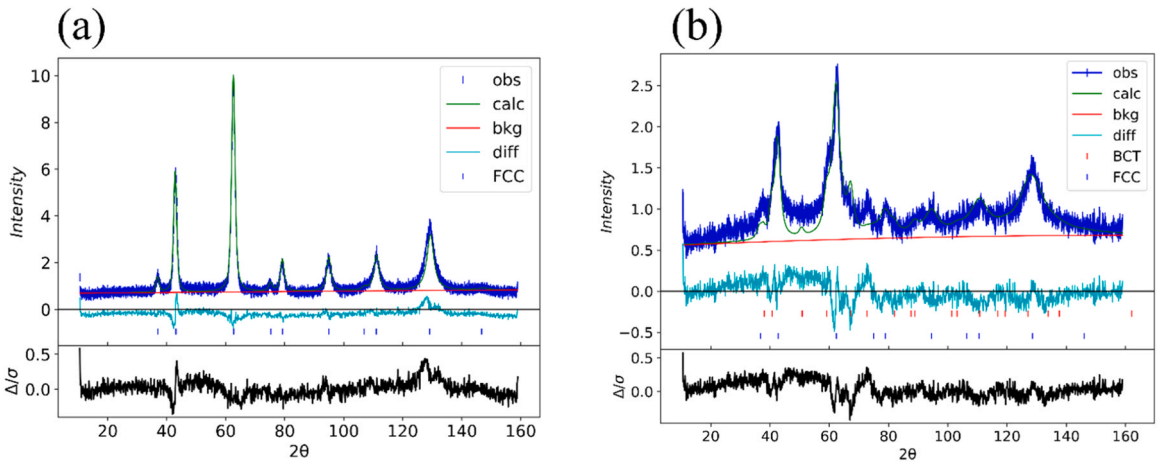

Fig. 7. Rietveld refinement of neutron diffraction pattern of TiNbVZr alloy at (a) 25 °C, and (b) 290 °C.

Table 4
Crystal parameters and deuterium occupation factor for TiNbVZr alloy at different temperatures.

Phase		25 °C	250 °C	290 °C	310 °C
FCC	a (Å)	4.518	4.526	4.535	4.531
	D_{occu}	1	1	1	1
	%	100	100	67	43
BCT	a (Å)	—	—	3.351	3.374
	c (Å)			3.979	3.850
	D_{occu}	—	—	0.6	0.6
	%	—	—	33	57

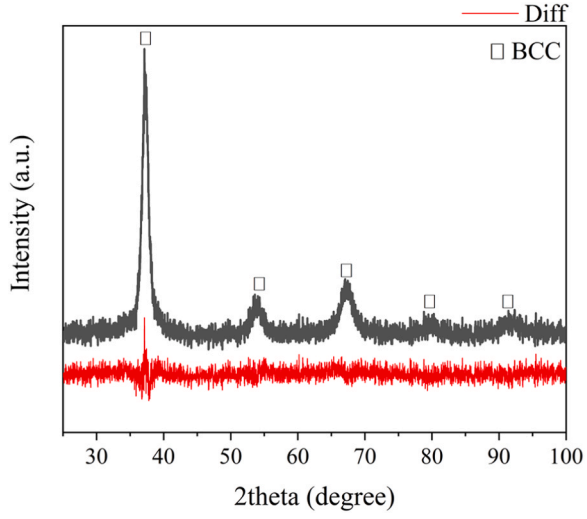

Fig. 8. XRD analysis of TiVZrNb (x = 1) dehydrided at 375 °C under dynamic vacuum.

Table 5
Lattice parameters and phase fraction of TiNbVZr alloy as cast, hydrided and dehydrided at 375 °C determined by X-ray diffraction. Error on the last significant digit is indicated between brackets.

Alloy state	Phase	Lattice parameter (Å)	Cell volume (Å^3)
As-cast	BCC	3.311 (2)	36.31 (3)
Fully hydrided	FCC	4.540 (1)	93.78 (8)
After *ex-situ* desorption	BCC	3.399 (1)	39.30 (5)

difference could be explained by the temperature and the pressure used in each dehydrogenation experiment. It is essential to acknowledge that a direct comparison between the two dehydrogenation experiments (by neutron diffraction and XRD) may be challenging due to differing desorption conditions. Notably, while the neutron diffraction pattern of the desorbed alloy was presented at 310 °C, the other underwent desorption at 375 °C. These variations in temperature could introduce substantial differences in desorption kinetics and behaviour, thereby complicating any straightforward comparison between the two results.

3.6. Neutron diffraction analysis of x = 0 (HfNbVZr) alloy: in-situ measurements

In-situ neutron diffraction patterns of HfNbVZr alloy during heating from 25 °C to 300 °C under dynamic vacuum are presented in Fig. 9. It is clear that there is an evolution of the crystal structure with temperature. To quantify this, Rietveld refinement was performed on all patterns.

As a representative of Rietveld refinement, Fig. 10 (a) and (b) shows the refined pattern of the alloy at 25 °C and 280 °C respectively. It can be seen that all the peaks of the pattern are matching well with an FCC and C15 Laves phases for the pattern at 25 °C, while for the pattern at 280 °C they correspond well with a BCT and C15 Laves phases.

The crystal structure refinements were carried out to acquire the occupation of deuterium atoms in the lattice and the refinement results are tabulated in Table 6. These refinements confirm that no desorption occurred before reaching 150°C, as the phase abundance stays constant.

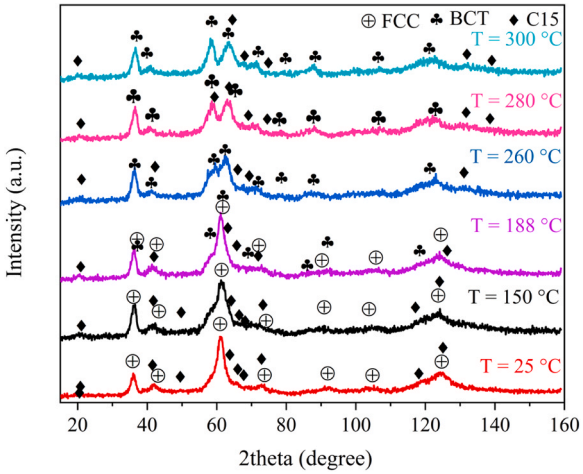

Fig. 9. Desorption neutron diffraction pattern of fully deuteried HfNbVZr alloy.

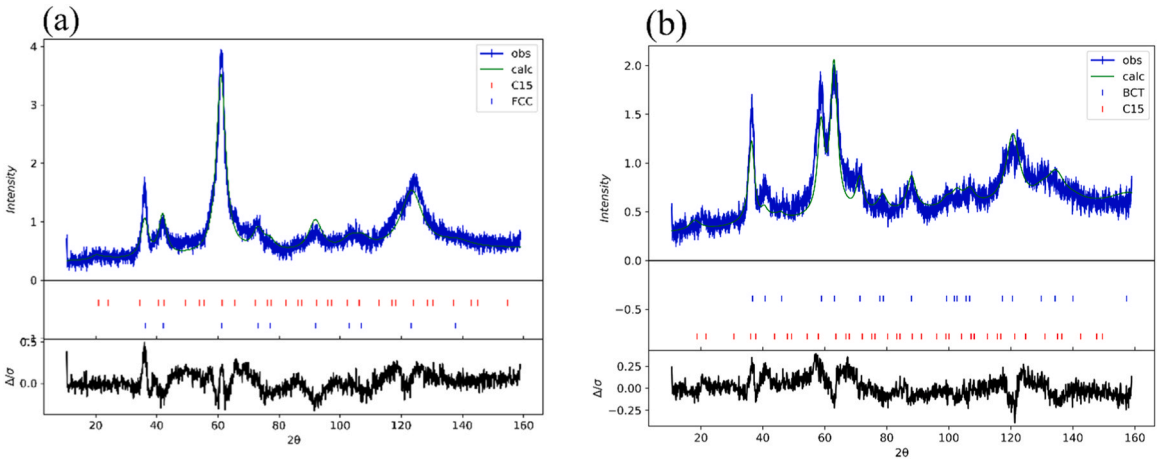

Fig. 10. Rietveld refinement of neutron diffraction pattern of HfNbVZr alloy at (a) 25 °C, and (b) 280 °C.

Table 6
Crystal parameters and deuterium occupation factor for HfNbVZr alloy at different temperatures.

Phase		25 °C	150 °C	188 °C	260 °C	280 °C	300 °C
FCC	a (Å)	4.642	4.659	4.671	4.665	-	-
	D_{occu}	1	1	1	1	-	-
	D/M = (D_{occ}*number of occupied sites) / number of metal atoms)	2	2	2	2	-	-
	Phase abundance (%)	84	82	25	15	-	-
BCT	a (Å)	-	-	3.462	3.415 4.224	3.409	3.417
	c (Å)	-	-	4.383		4.277	4.184
	D_{occu}	-	-	0.59	0.57	0.58	0.55
	D/M	-	-	1.18	1.1	1.2	1.1
	%	-	-	65	70	91	85
C15	a (Å)	7.874	7.988	7.994	7.982	7.910	7.770
	D_{occu}	0.42	0.39	0.36	0.32	0.32	0.21
	D/M	-	-	1.4	1.3	1.3	0.8
	%	16	17	8	15	9	14

Between 150 °C and 88°C, the FCC structure starts to release hydrogen, leading to the formation of the monohydride BCT with a D/M ratio of 1.2. With increasing temperature, the FCC structure entirely transforms into the monohydride BCT, where the D/M ratio remains constant.

The C15 Laves phase also undergoes hydrogen desorption, prompted by a reduction in the D/M ratio from 1.68 at 25 °C to 1.44 at 188 °C. Furthermore, in the C15 phase, the lattice parameter diminishes in response to the decrease of deuterium content. The C15 phase releases hydrogen, resulting in a final D/M ratio of 0.84 at 300 °C.

3.7. X-ray Diffraction analysis of x = 0 (HfNbVZr) alloy: ex-situ dehydrogenation

For the HfNbVZr alloy, a dehydrogenation experiment (*i.e.* dynamic vacuum for two hours at 375 °C) was conducted followed by *ex-situ* XRD analysis to complementarily investigate the dehydrogenation process. The XRD analysis of the dehydrogenated sample is presented in Fig. 11. The crystal parameters of as-cast, fully hydrided and desorbed HfNbVZr alloy are reported in Table 7.

For the HfNbVZr alloy ($x = 0$), two phases (BCC and C15) are present after the dehydrogenation experiment, as reported in the as cast state. Also an unidentified peak is present at 34.2°. The unit cell volume of the BCC phase after dehydrogenation as determined by the Rietveld refinement, is 42.97 Å^3. This volume is larger than that of the BCC in the as cast state (39.06 Å^3). For the C15 phase, the unit cell volume after desorption (446.33 Å^3) is also larger than the one for the C15 in the as cast state (419.8 Å^3). This indicated that the BCC and the C15 are not fully dehydrided and still contains hydrogen. An estimation of the hydrogen content can be done assuming a volume of hydrogen atom of 2.7 Å^3. Then, the amount of hydrogen retained in the BCC phase is

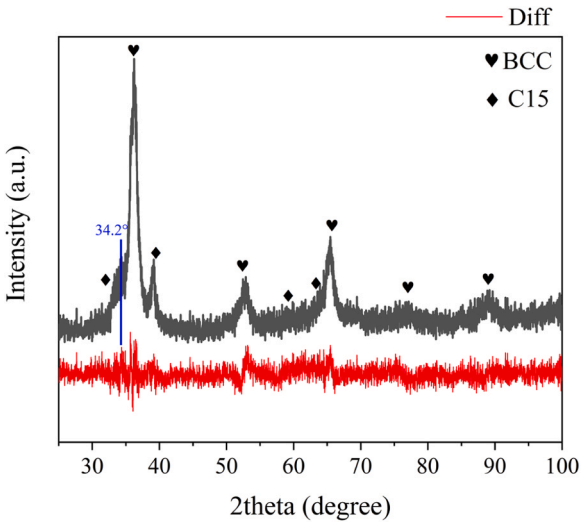

Fig. 11. XRD analysis of HfVZrNb (x = 0) dehydrided at 375 °C under dynamic vacuum.

estimated to be around 0.67 wt%.

Upon comparing the two alloys post-dehydrogenation through *in-situ* neutron diffraction and *ex-situ* XRD analyses, a noticeable distinction arises: during *ex-situ* dehydrogenation, the alloy exhibits greater hydrogen desorption, accompanied by the formation of the BCC phase, a phenomenon not observed in the *in-situ* dehydrogenated alloy. This could be caused by the difference in the applied desorption conditions

Table 7
Lattice parameters and phase fration of HfNbVZr alloy as cast, hydrided and dehydrided at 375°C determined by X-ray diffraction. Error on the phase fractions is ±1, and on the last significant digit is indicated between brackets.

Alloy state	Phase	Phase fraction (%)	Lattice parameter (Å)	Cell volume (Å^3)
As-cast	BCC	85	3.393 (1)	39.06 (2)
	C15	15	7.488 (2)	419.8 (4)
Fully hydrided	FCC	87	4.653 (3)	100.7 (2)
	C15	13	7.939 (5)	500.5 (1)
After *ex-situ* desorption	BCC	85	3.503 (1)	42.97 (2)
	C15	15	7.642 (3)	446.3 (5)

used in these two methods. As previously said, it is important to note that direct comparison between the two alloys may not be appropriate due to variations in desorption conditions. Specifically, one alloy underwent desorption at 300 °C, while the other was desorbed at 375 °C. Such temperature disparities could exert a significant influence on the desorption behavior.

4. Conclusions

The hydrogen storage properties of $Hf_{1-x}Ti_xNbVZr$ BCC high entropy alloys synthesized by arc melting have been investigated and the following observations were made:

1. The substitution of Hf by Ti in the $Hf_{1-x}Ti_xNbVZr$ alloys presents interesting results for enhancing hydrogen storage capacities. The H/M ratio is constant upon substitution of Hf by Ti but, because of the lighter atomic weight of Ti, the gravimetric capacity increased.
2. X-ray diffraction and neutron analyses elucidate the structural evolution during dehydrogenation processes, revealing phase transitions and hydrogen occupancy within lattice sites. Notably, the alloys exhibit multiphase behavior during dehydrogenation, with some phases remaining incompletely desorbed even after extensive dehydrogenation treatments.
3. *In-situ* neutron diffraction analysis during dehydrogenation reveals the temperature-dependent desorption behavior of the alloys. It is observed that the desorption of HfNbVZr initiates at temperatures lower than that of TiNbVZr alloy. The *in-situ* neutron diffraction experiments during deuterium desorption seems to indicate a two-step phase transition first from FCC dihydride to BCT monohydride and second from BCT to BCC.

These findings can significantly advance research aimed at designing novel and high-performing High-Entropy Alloys (HEAs) for solid-state energy storage applications.

Funding

This research was funded in parts from a NSERC discovery grant. The region Nouvelle aquitaine in France and the UQTR in canad ahas funded the thesis to accomplish this work.

CRediT authorship contribution statement

Lambert van Eijck: Writing – review & editing, Validation, Investigation, Conceptualization. **Maria Moussa:** Writing – review & editing, Writing – original draft, Validation, Investigation, Formal analysis, Conceptualization. **Jean-Louis Bobet:** Writing – review & editing, Visualization, Validation, Supervision, Resources, Methodology, Funding acquisition, Formal analysis, Conceptualization. **Jacques Huot:** Writing – review & editing, Validation, Supervision, Resources, Project administration, Methodology, Investigation, Funding acquisition, Formal analysis, Conceptualization.

Declaration of Competing Interest

The authors declare that they have no known competing financial interests or personal relationships that could have appeared to influence the work reported in this paper.

Acknowledgments

The authors thank the Region Nouvelle Aquitaine and the Canadian government for financial support to this work through a PhD grant.

Appendix A. Supporting information

Supplementary data associated with this article can be found in the online version at doi:10.1016/j.jallcom.2024.177103.

Data availability

Data will be made available on request.

References

[1] Sonja Studer, Samuel Stucki, John D. Speight, Hydrogen as a Fuel in: ZÜTTEL, Andreas, BORGSCHULTE, Andreas, et SCHLAPBACH, Louis. Hydrogen as a future energy carrier. 2008. https://doi.org/10.1002/9783527622894.ch3.
[2] Ulrich Eberle, Michael Felderhoff, Ferdi Schueth, Chemical and physical solutions for hydrogen storage, Angew. Chem. Int. Ed. 48 (36) (2009) 6608–6630, https://doi.org/10.1002/anie.200806293.
[3] Brain Cantor, et al., Microstructural development in equiatomic multicomponent alloys, Mater. Sci. Eng.: A 375 (2004) 213–218, https://doi.org/10.1016/j.msea.2003.10.257.
[4] J.-W. Yeh, et al., Nanostructured high-entropy alloys with multiple principal elements: novel alloy design concepts and outcomes, Adv. Eng. Mater. 6 (5) (2004) 299–303, https://doi.org/10.1002/adem.200300567.
[5] Q. Ding, Y. Zhang, X. Chen, et al., Tuning element distribution, structure and properties by composition in high-entropy alloys, Nature 574 (2019) 223–227, https://doi.org/10.1038/s41586-019-1617-1.
[6] Felipe Marques, et al., Review and outlook on high-entropy alloys for hydrogen storage, Energy Environ. Sci. 14 (10) (2021) 5191–5227, https://doi.org/10.1039/D1EE01543E.
[7] Daniel B. Miracle, Oleg N. Senkov, A critical review of high entropy alloys and related concepts, Acta Mater. 122 (2017) 448–511, https://doi.org/10.1016/j.actamat.2016.08.081.
[8] Zlotea, Claudia, et al. "Compositional effects on the hydrogen storage properties in a series of refractory high entropy alloys." *Fron.*
[9] Z. Yu, Y. Yan, J. Qiang, W. Gao, X. Wang, X. Liu, W. Du, Microstructure evolution and compressive property variation of AlxCoCrFeNi high entropy alloys produced by directional solidification, Intermetallics 152 (2023) 107749.
[10] P.P. Bhattacharjee, G.D. Sathiaraj, M. Zaid, J.R. Gatti, C. Lee, C. Tsai, J. Yeh, Microstructure and texture evolution during annealing of equiatomic CoCrFeMnNi high-entropy alloy, J. Alloy. Compd. 587 (2014) 544–552.
[11] Yuh Fukai, The metal-hydrogen system: basic bulk properties, Vol. 21, Springer Science & Business Media, 2006.
[12] Martin Sahlberg, et al., Superior hydrogen storage in high entropy alloys, Sci. Rep. 6 (1) (2016) 36770, https://doi.org/10.1038/srep36770.
[13] Magnus Moe Nygård, et al., Hydrogen storage in high-entropy alloys with varying degree of local lattice strain, Int. J. Hydrog. Energy 44 (55) (2019) 29140–29149, https://doi.org/10.1016/j.ijhydene.2019.03.223.
[14] Gustav Ek, et al., Elucidating the effects of the composition on hydrogen sorption in TiVZrNbHf-based high-entropy alloys, Inorg. Chem. 60 (2) (2020) 1124–1132, https://doi.org/10.1021/acs.inorgchem.0c03270.
[15] Huahai Shen, et al., Compositional dependence of hydrogenation performance of Ti-Zr-Hf-Mo-Nb high-entropy alloys for hydrogen/tritium storage, J. Mater. Sci. Technol. 55 (2020) 116–125, https://doi.org/10.1016/j.jmst.2019.08.060.
[16] Von Colbe, Jose Bellosta, et al., Application of hydrides in hydrogen storage and compression: Achievements, outlook and perspectives, Int. J. Hydrog. Energy 44 (15) (2019) 7780–7808, https://doi.org/10.1016/j.ijhydene.2019.01.104.
[17] J.W. Zhang, et al., Composition and temperature influence on hydrogenation performance of TiZrHfMo x Nb 2–x high entropy alloys, J. Mater. Chem. A 11 (38) (2023) 20623–20635, https://doi.org/10.1039/D3TA01990J.
[18] R. Floriano, G. Zepon, K. Edalati, A. Mohammadi, Hydrogen storage properties of new A3B2-type TiZrNbCrFe high-entropy alloy, Int. J. Hydrog. Energy 46 (2021) 23757–23766.
[19] T.P. Yadav, S. Mukhopadhyay, S.S. Mishra, N.K. Mukhopadhyay, O.N. Srivastava, Synthesis of a single phase of high-entropy Laves intermetallics in the Ti–Zr–V–Cr–Ni equiatomic alloy, Philos. Mag. Lett. *97* (12) (2017) 494–503, https://doi.org/10.1080/09500839.2017.1418539.

[20] Daniel B. Miracle, Oleg N. Senkov, A critical review of high entropy alloys and related concepts, Acta Mater. 122 (2017) 448–511, https://doi.org/10.1016/j.actamat.2016.08.081.
[21] A. Bruker, Topas V3: general profile and structure analysis software for powder diffraction data–user's manual; Bruker AXS, Karlsruhe; Coehlo AA (2007) TOPAS academic. Coelho Software, Brisbane, in, 2005.
[22] L. Van Eijck, et al., Design and performance of a novel neutron powder diffractometer: PEARL at TU Delft, J. Appl. Crystallogr. 49 (5) (2016) 1398–1401, https://doi.org/10.1107/S160057671601089X.
[23] Brian H. Toby, Robert B. Von Dreele, GSAS-II: the genesis of a modern open-source all purpose crystallography software package, J. Appl. Crystallogr. 46 (2) (2013) 544–549, https://doi.org/10.1107/S0021889813003531.
[24] Maria Moussa, et al., Effect of the synthesis route on the microstructure of HfxTi (1− x) NbVZr refractory high-entropy alloys, Metals 13 (2) (2023) 343, https://doi.org/10.3390/met13020343.
[25] Salma Sleiman, Jacques Huot, Microstructure and First Hydrogenation Properties of TiHfZrNb1− xV1+ x Alloy for x= 0, 0.1, 0.2, 0.4, 0.6 and 1, Molecules 27 (3) (2022) 1054, https://doi.org/10.3390/molecules27031054.
[26] H. Peisl, Lattice strains due to hydrogen in metals, Hydrog. Met. I: Basic Prop. (2005) 53–74.
[27] Salma Sleiman, Jacques Huot, Effect of particle size, pressure and temperature on the activation process of hydrogen absorption in TiVZrHfNb high entropy alloy, J. Alloy. Compd. 861 (2021) 158615, https://doi.org/10.1016/j.jallcom.2021.158615.
[28] Dennis Karlsson, et al., Structure and hydrogenation properties of a HfNbTiVZr high-entropy alloy, Inorg. Chem. 57 (4) (2018) 2103–2110, https://doi.org/10.1021/acs.inorgchem.7b03004.
[29] Jean-Louis Soubeyroux, et al., Phase stability and neutron diffraction studies of Laves phases Zr (Cr1− xMx) 2 with M=(Cu0. 5Ni0. 5) and 0< x< 0.2 and their hydrides, J. Alloy. Compd. 231 (1-2) (1995) 760–765, https://doi.org/10.1016/0925-8388(95)01714-3.
[30] D.G. Westlake, S.T. Ockers, Thermal expansion of vanadium and vanadium hydride at low temperature, J. Less Common Met. 22 (2) (1970) 225–230, https://doi.org/10.1016/0022-5088(70)90023-8.